On-site catalytic wastewater remediation by sustainably produced H$_2$O$_2$ via scalable single-atomic Fe-incorporated Janus membrane

Yuhan Wu [a,b], Yifei Wang [c,*], Ruyan Chen [a], Jiaqing Xu [a], Yifei Wang [a], Hangyuan Zhang [a], Yifan Ding [b], Beibei Li [c], Shuying Dong [a,*], Shixue Dou [d,e], Xiao Zhang [f,*], Jingyu Sun [b,*], Jianhui Sun [a,*]

[a] School of Environment, Key Laboratory for Yellow River and Huai River Water Environmental and Pollution Control-Ministry of Education, Henan Normal University, Xinxiang 453007, PR China
[b] College of Energy, Soochow Institute for Energy and Materials Innovations, Jiangsu Provincial Key Laboratory for Advanced Carbon Materials and Wearable Energy Technologies, Soochow University, Suzhou 215006, PR China
[c] National Engineering Laboratory for Advanced Municipal Wastewater Treatment and Reuse Technology, Key Laboratory of Beijing for Water Quality Science and Water, Environment Recovery Engineering, Beijing University of Technology, Beijing 100124, PR China
[d] Institute of Energy Material Science, University of Shanghai for Science and Technology, Shanghai 200093, PR China
[e] Institute for Superconducting and Electronic Materials, University of Wollongong, Innovation Campus, Wollongong, New South Wales 2500, Australia
[f] Department of Mechanical Engineering, The Hong Kong Polytechnic University, Hung Hom, Kowloon, Hong Kong, PR China

ARTICLE INFO

ABSTRACT

Electrosynthesis of hydrogen peroxide (H$_2$O$_2$) from oxygen is a green and sustainable route toward on-site wastewater treatment. Nevertheless, the performance mismatch of the catalyst species and gas-diffusion components gives rise to low O$_2$ utilization efficiency and limited H$_2$O$_2$ production rate in a practical cell. Herein, we propose a flexible and scalable Janus electrode comprising hydrophilic single-atomic Fe-incorporated catalytic layer and hydrophobic gas-attraction layer. The hydrophobic layer enables efficient oxygen diffusion, and the hollow-structured catalysts allow oxygen gas trapping with a high local oxygen concentration, resulting in a high Faradaic efficiency and fast H$_2$O$_2$ production rate. Accordingly, an 80 h electrocatalytic H$_2$O$_2$ synthesis could be gained at 80 mA cm^{-2}. The Janus electrode delivers a H$_2$O$_2$ selectivity of 92% and a yield of 592 mmol g^{-1} h^{-1} in a flow cell. The thus-produced H$_2$O$_2$ allows for an *in situ* antibiotic removal, with the potential for on-site eco-restoration.

1. Introduction

Hydrogen peroxide (H$_2$O$_2$) is a green chemical species that is broadly utilized in the field of environmental protection and medical disinfection. Commercial production of H$_2$O$_2$ mainly relies upon large-scale anthraquinone oxidation since the 1940 s, wherein the transportation and storage of highly-concentrated H$_2$O$_2$ would pose serious safety issues [1–4]. Recently, oxygen electrochemistry throughout two-electron (2e$^-$) reduction pathway has emerged as an attractive strategy to allow on-demand H$_2$O$_2$ production, which is accompanied by collective advantages including eco-friendliness and cost-effectiveness toward positive environmental implications [2,5–7].

To steer oxygen reduction reaction (ORR) to H$_2$O$_2$ through the two-electron pathway, a multitude of electrocatalysts, including noble metals (Pt, Au, Pd, Pd-Hg, and Au-Pd) and their alternatives (doped carbon materials, transition metal compounds, and their hybrids), have been widely exploited [8–12]. Despite these efforts, the improvements in the activity and selectivity of electrocatalysts met with limited success. In this sense, the unique geometry merit and high atom utilization of single-atom catalysts render them ideal candidates for the H$_2$O$_2$ generation *via* 2e$^-$ ORR [13–15]. The electronic structure of atomically dispersed M–N–C materials can be tuned by many parameters, such as the metal center, coordination element, and/or surrounding matrix composition, which give rise to optimized catalytic performance [16–19]. For instance, a Co–N$_4$ decoration in the framework of oxygen-incorporated nitrogen-doped graphene showcased a promising

electrochemical H_2O_2 productivity of 418 ± 19 mmol $g_{cat}^{-1}h^{-1}$ (at 50 mA). Despite these conspicuous advancements, it is noted that most of the reported single-atom catalysts have been employed in their powdery forms and evaluated in rotating ring−disk electrode (RRDE) configurations at small current densities, which could hardly reflect the catalytic effectiveness in any practical operation under working conditions [20–23].

In practical gas-electrode−electrolyte catalytic modes, integrating active catalysts with sufficient oxygen supply is crucial, but typically deficient owing to the low solubility (0.9 mM at 298 K/1 atm pressure) and sluggish O_2 diffusion rate in solution [24]. To this end, constructing an effective gas-diffusion electrode (GDE) to augment the O_2 mass transfer efficiency is an appealing practice, which allows the direct supply of oxygen to the cathode surface from the ambient without the need of transport *via* dissolution [25–28]. A more accessible electroactive region, featured by a solid−liquid−gas three-phase catalytic interface, is thus formed. Zhang *et al.* pioneered the GDE design by employing modified graphite felt, readily boosting the H_2O_2 productivity by nearly ten folds [29]. Very recently, Lin and colleagues successfully demonstrated the free-standing GDE fabrication by assembling Co single atoms and vertical graphene arrays, which sustained a record-breaking H_2O_2 productivity without significant decay over 36 h [30]. To broaden the designing concept of GDEs and explore the related applications toward on-site environmental treatment, further investigation on high-performance GDE equipped with single-atom catalytic moieties is meaningful and desirable. Inspired by these aspects, the present work reports a Janus electrode with asymmetric surface features to render sufficient reaction species to expedite the gas diffusion process. Single-atomic Fe-decorated nitrogen-rich carbon nanosphere (CNS) arrays as electrocatalysts are expected to facilitate charge transfer without sacrificing the mass transport efficiency. The thus-produced H_2O_2 satisfies an *operando* antibiotic and dye removal, with the potential for on-site eco-restoration.

Herein, we constructed a Janus working electrode with asymmetric surface features to render sufficient reaction species to expedite the gas diffusion process. Dispersed atomic Fe-decorated nitrogen-rich carbon nanosphere arrays as efficient electrocatalysts could facilitate fast charge transfer without sacrificing the mass transport efficiency. Benefiting from the superaerophilicity feature, the three-phase electrode architecture achieves a high selectivity of $2e^-$ ORR (92%). More encouragingly, thus-produced H_2O_2 satisfies an *operando* antibiotic and dye degradation, holding practical promise for on-site wastewater remediation.

2. Experimental section

2.1. Material synthesis

The synthesis of single-atomic Fe dispersed nitrogen-rich carbon nanosphere (doped by oxygen) [Fe-CNS(O)] was carried out *via* an impregnation-reduction method. In a typical procedure, iron acetate (10.2 mg) was first dissolved in 10 mL ethanol. The prepared CNS(O) precursor (80 mg) was dispersed into the above mixture and subsequently heated at 80 °C for 240 min. The product was then collected and annealed at 500 °C for 120 min. The thus-formed powder was then treated in 25% acetic acid solution for 180 min. Upon washing alternatively in deionized water and ethanol, the powder was dried in a vacuum overnight to result in Fe-CNS(O). To prepare the Fe-CNS, similar synthetic steps were adopted, except for using the CNS as the precursor.

2.2. Fabrication of Fe-CNS(O) Janus GDE

The commercial carbon felt (1×1 cm^2) was cleaned in deionized water and ethanol in turn by ultrasonic cleaning for 15 min and dried under vacuum. A polytetrafluoroethylene (PTFE) suspension (6 wt%, 500 μL) and prepared catalyst ink was sprayed on each side of the cleaned carbon felt, respectively. It was naturally air-dried at room temperature and then calcined at 350 °C for 120 min. The configured catalyst ink was in fact a catalyst slurry, which consisted of a mixture of deionized water (240 μL), isopropyl alcohol (200 μL), PTFE (10 μL), Nafion (50 μL) and the catalyst.

2.3. Continuous production of H_2O_2 in a flow cell

Bulk H_2O_2 production was carried out in a customized flow cell. 0.5 mg cm^{-2} Fe-CNS(O) loaded onto a 1×1 cm^2 Janus GDE as ORR cathode, and 0.2 mg cm^{-2} IrO_2 was used as anode for water oxidation. Nafion 117 was employed to function as a proton exchange membrane. 0.1 M KOH was used as the one-pass flowing catholyte to carry as-synthesized H_2O_2 out at a flexible rate of 120 mL h^{-1} dictated by a peristaltic pump, while the anolyte of 0.5 M H_2SO_4 solution could be recycled. The electrochemical response was recorded by an electrochemical workstation (CHI 760E, CH Instrument, USA). The cell voltage kept the real operation value without *iR* compensation. The other experimental procedures pertaining to the synthesis of CNS and CNS(O), instrumental characterizations, electrochemical evaluation, H_2O_2 concentration measurement (the cerium sulfate titration method and related Ref. therein), theoretical calculations and analysis of degradation intermediates are provided in Supplementary Methods in the Supporting Information file.

3. Results and discussion

3.1. Construction of single-atomic Fe-incorporated Janus GDE

As illustrated in Fig. 1**a**, our Janus GDE is based upon the employment of commercial carbon felt, whose one side is modified by PTFE to form a gas-attraction layer. Such a layer is witnessed by hydrophobic nature, which is beneficial to acquiring its superaerophilicity. At the other side, the prepared Fe-CNS(O) is subject to spray-coating to form a catalytic layer with obvious hydrophilicity. A carbonization procedure was used to prepare bare CNS, using a silica nanosphere as the hard template. The as-constructed GDE thus affords different surface properties. In addition, the size and thickness could be customized according to the application specifications, highlighting the flexibility and scalability of our Janus GDE (Fig. 1**b**). To examine the sandwich structure of the electrode, cross-sectional scanning electron microscopy (SEM) was utilized, clearly showing the gas-attraction layer, the transport layer, and the catalytic layer (Fig. 1**c**). Fig. 1**d** displays the detailed morphology of a typical carbon fiber mat, showing an inter-connected network with discernible porosity (Fig. S1, Supporting Information). In this sense, the steric hindrance for air mass transport throughout the GDE is extremely low, enabling the active oxygen diffusion to the catalytic interface. Upon the material modification, representative carbon fiber presents uniform coating of either PTFE or Fe-CNS(O), where the surface wettability tests by static water contact angle measurements imply the hydrophobicity and hydrophilicity, respectively (Figs. 1**e and** 1**f**). Such a Janus surface property could also be evidenced by simple visualization experiments, where the presence of gas pockets in the case of hydrophobic surface is conspicuous in contrast to that of hydrophilic counterpart (Fig. S2).

To showcase the air-adsorption capability of the Janus GDE, gas adsorption experiments were performed by specifically fixing the gas-attraction layer and immersing it in the electrolyte solution, where a set-up optical microscopy could inspect in a cross-sectional manner. This would allow the *in situ* optical microscopy observation to monitor the real-time surface changes of the gas-attraction layer in the electrolyte during certain aeration process. As for the original carbon felt electrode, a snapshot at the beginning of aeration indicates no noticeable change (Fig. 2**a**, left panel). By contrast, the modified electrode manifests a clear enrichment of gas pockets (Fig. 2**a**, central and right panels), which was imaged at identical conditions. In further contexts, the aerophilic feature
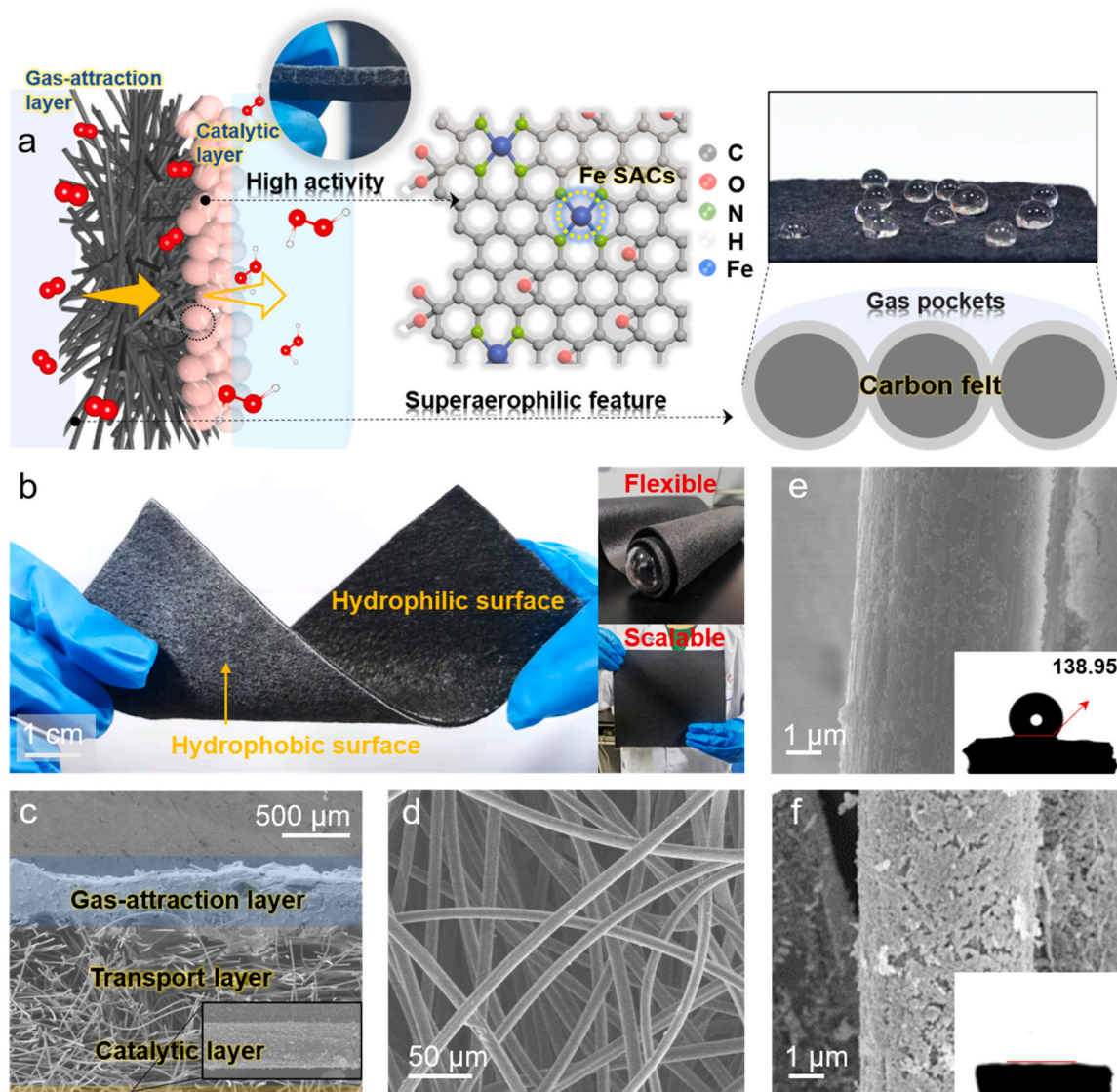
Fig. 1. Schematic illustration and structure characterization of as-prepared Janus electrode. (a) Schematic illustration of the Janus GDE and solid–liquid–gas interfaces during ORR. The as-constructed GDE affords different surface properties with a hydrophobic gas diffusion layer and a hydrophilic single-atom Fe-CNS(O) catalytic layer. (b) Photograph of the prepared Janus electrodes, demonstrating the flexibility and scalability. (c) Cross-sectional SEM image of the Fe-CNS(O) Janus electrode. (d) SEM image of the original carbon felt. (e) SEM image and contact angle graph (inset) of PTFE-coated carbon felt. (f) SEM image and contact angle graph (inset) of Fe-CNS(O)-modified carbon felt.

of the modified electrode was evaluated by the adhesion behavior of supplied O_2 bubbles. To this end, the O_2 flow rate was controlled at 0.1 mL min^{-1}, where an individual bubble with a volume of *ca.* 0.5 μL was released in the electrolyte. As witnessed in Fig. 2**b**, the shape evolutions of an individual bubble on-touch the electrode surfaces were captured by the time-resolved camera from 0 to 30 ms. It is evident that the designed electrode upon aerophilic treatment enables good uptake of foreign bubbles in comparison with the scenario of original electrode. Once the bubble touches the aerophilic surface, it immediately integrates into the pre-formed gas pockets at the electrode-electrolyte interface. This would be favorable to offer a steady stream of reactants for the catalytic reaction.

To gain theoretical insight into the mass transfer effect of the Fe-CNS (O) catalytic layer, finite element method performed by COMSOL Multiphysics was applied to simulate the distributions of O_2/H_2O_2 concentration and local current density at the electrode/electrolyte interface [31,32]. ORR occurs typically at the interfacial region of the catalyst owing to the sluggish mass transport rate of O_2 [33]. Therefore, the concentration and related distribution of reactants at the interface is

critical. By rationalizing the catalyst geometry of our Fe-CNS(O) reactor, uniform O_2 flux is expected to benefit from the arc shape interspersed by metal dispersions (Fig. S3) [34,35]. As depicted in Fig. 2**c**, the initial states of dissolved oxygen when approaching the interface are distinct for the cases of bare CNS and Fe-CNS(O). As such, oxygen enrichment occurs at Fe-CNS(O) on the premise of the other modeling parameters kept identical, suggesting that the optimized catalyst configuration is in favor of O_2 adsorption. Meanwhile, confining sufficient reactive species to the interior and near-surface regions of catalysts would augment conversion efficiencies of O_2 to H_2O_2 and hence facilitate their utilization. In the case of H_2O_2 formation, the initial current density of Fe-CNS (O) is stronger than that of bare CNS; When the catalytic reaction is stabilized, the content of H_2O_2 enriched at the Fe-CNS(O) remains much higher (Fig. 2**d**).

3.2. Preparation and characterization of Fe-CNS(O) catalyst

The catalyst plays a key role in determining the functionality of the Janus GDE and the 2e$^-$ ORR performance. The Fe-CNS(O) single atom
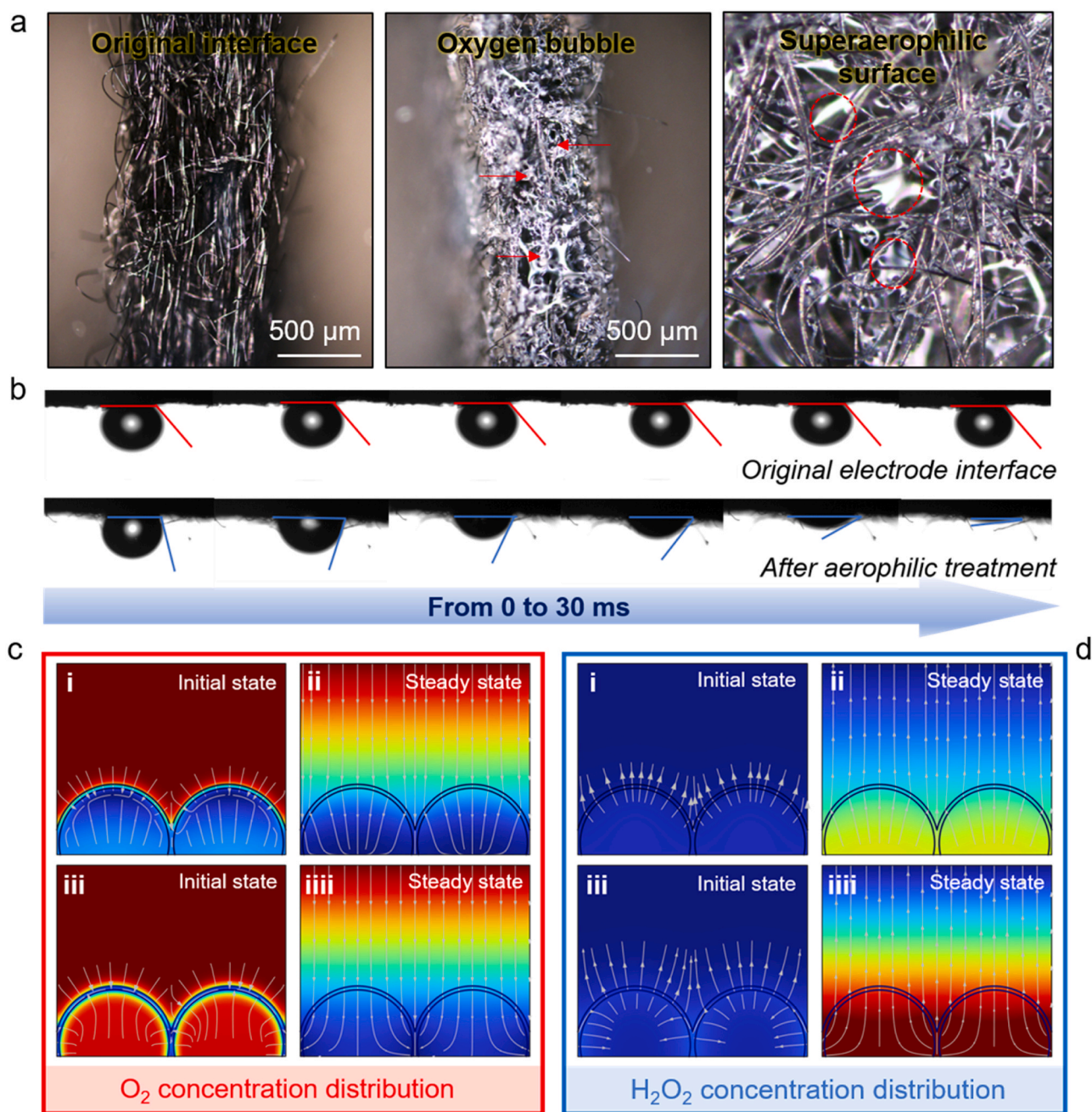
Fig. 2. Experimental observation and theoretical simulation of local oxygen at the Janus electrode. (a) The real-time cross-sectional optical microscopy images of different gas-attraction layers immersed in the aqueous electrolyte during aeration process: original carbon felt surface (left panel), after aerophilic modifications (central panel) and enlarged view of aerophilic carbon felt surface (right panel). (b) The shape evolutions of an individual bubble on the surface of modified and unmodified electrodes as a function of time. (c and d) The flux profiles of O_2 and H_2O_2 at the near interface, obtained by finite element simulation on the structure corresponding to the catalyst. The red wireframe (c) is the O_2 concentration distribution (i and ii: initial and steady state of CNS; iii and iiii: initial and steady state of Fe-CNS(O)). The blue wireframe (d) is the concentration distribution of the generated H_2O_2 (i and ii: initial and steady state of CNS; iii and iiii: initial and steady state of Fe-CNS(O)).

catalyst was designed in the pursuit of favorable activity and selectivity toward $2e^-$ ORR. The morphological information of as-synthesized Fe-CNS(O) was acquired by SEM and transmission electron microscopy (TEM). The top-view SEM images reveal well-defined sphere architectures with a uniform size distribution (Fig. 3a; Fig. S4). The TEM observation in Fig. 3b highlights the hollow architecture of Fe-CNS(O), showing a typical wall thickness of ~20 nm (Fig. S5). Corresponding element mapping under scanning TEM (STEM) mode denote homogeneous dispersions of C, N, O and Fe elements across the spherical structure (Fig. 3c). X-ray diffraction (XRD) patterns of bare CNS and Fe-

CNS(O) samples exhibit broadened carbon peaks without the trace of any metal signals (Fig. S6) [36,37]. The collected Raman spectra display a similar intensity ratio of D and G bands (I_D/I_G) for CNS and Fe-CNS(O), indicative of their comparable defect contents (Fig. S7). Moreover, the N_2 adsorption/desorption isotherm implies that Fe-CNS(O) harvests a Brunauer–Emmett–Teller specific surface area of 461 m^2 g^{-1}; The pore-size distributions indicate the mesopore formation with the pore size centering at ~4.3 nm (Fig. S8). Such a porous architecture is conducive to the exposure of active sites to the accessible reactive species and offer efficient pathways for mass transport [38,39]. The Fe
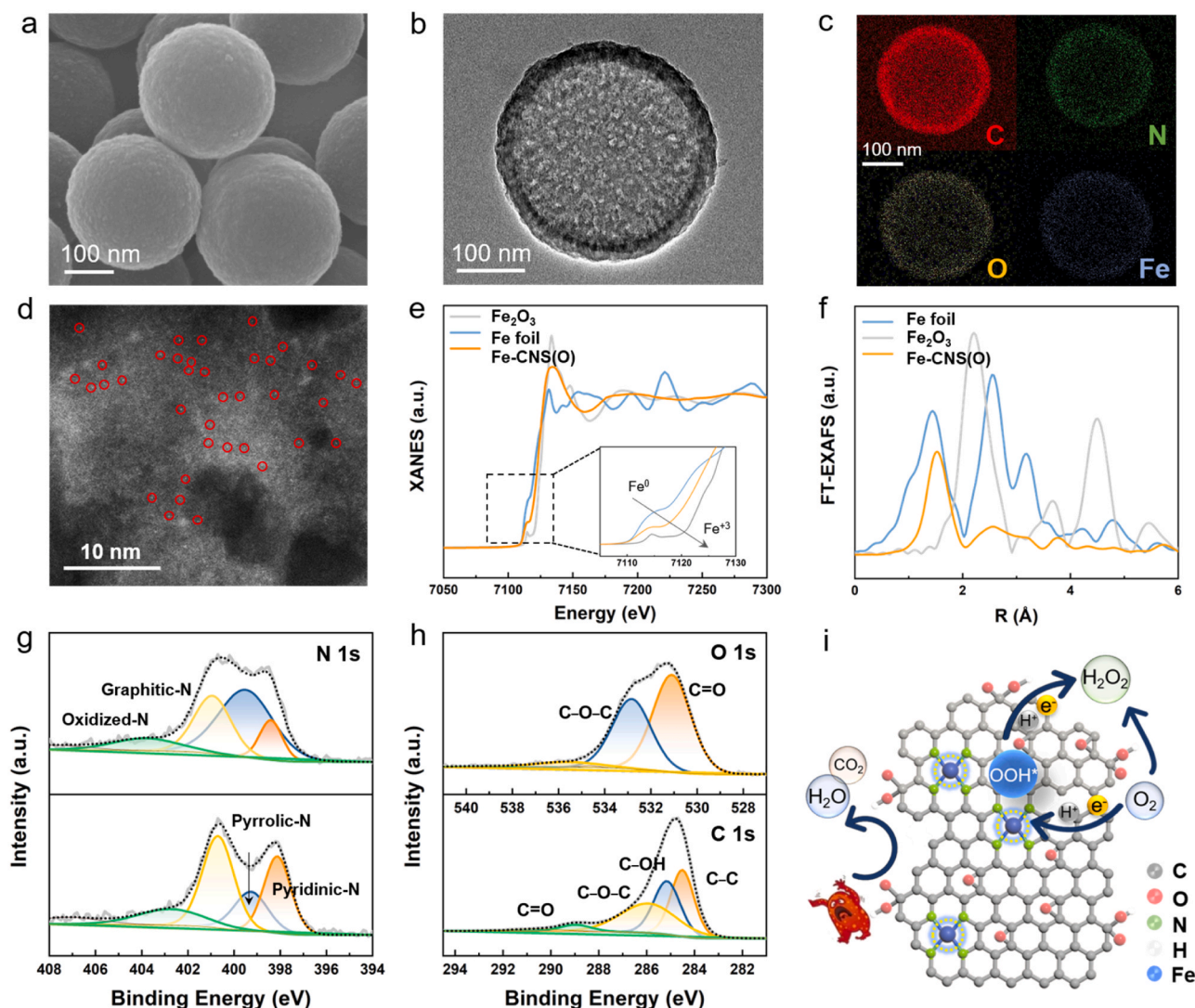
Fig. 3. Morphology and structure characterizations of the Fe-CNS(O) catalyst. (a and b) SEM and TEM images of the Fe-CNS(O). (c) EDS mapping of Fe-CNS(O), showing a homogeneous distribution of the C, N, O, and Fe elements. Scale bars: 100 nm. (d) HAADF-STEM image of Fe-CNS(O). (e and f) The Fe K-edge XANES spectra and corresponding FT-EXAFS curves for Fe-CNS(O) and Fe reference materials. (g) High-resolution N 1 *s* XPS spectra of CNS and Fe-CNS(O). (h) High-resolution O 1 *s* and C 1 *s* XPS spectra of Fe-CNS(O). (i) The proposed structure of FeN$_4$ site in Fe-CNS(O).

loading in the Fe-CNS(O) reached 1.6 wt% determined by inductively coupled plasma-atomic emission spectroscopy (Table S1).

High-angle annular dark-field scanning transmission electron microscopy (HAADF-STEM) inspection of Fe-CNS(O) reveals that the Fe species are atomically dispersed throughout the carbon nanocage frameworks (Fig. 3**d**). To probe the local chemical state and geometrical structure of Fe species within the prepared Fe-CNS(O) material, K-edge X-ray absorption near edge structure (XANES) and the relevant Fourier-transform extended X-ray absorption fine structure (FT-EXAFS) spectra were collected. As shown in Fig. 3**e**, the absorption edge position of the Fe-CNS(O) is located between those of Fe foil and Fe$_2$O$_3$, indicating that the Fe in Fe-CNS(O) is positively charged and might possess an average valence state locating in between 0 and + 3. The Fe K-edge FT-EXAFS spectrum presents the light scattering signal nearest neighbors at 1.46 Å (Fig. 3**f**), which is associated with the Fe–N scattering pair analogous to the tetrahedrally coordinated Fe (*i.e.*, Fe–N$_4$) [39–42] (Table S2). Notably, compared to the FT-EXAFS profile of Fe foil, no Fe–Fe coordination peak (at 2.2 Å) could be observed in the case of Fe-CNS(O), which echoes well with the XRD results to verify no formation of Fe nanoparticles or clusters.

The surface compositions of the Fe-CNS(O) were additionally

investigated using X-ray photoelectron spectroscopy (XPS). The survey spectrum shows the existence of C, N, O, and Fe elements (Fig. S9a) [40]. As for the Fe 2*p* XPS spectrum, two peaks located at 710.2 and 724.0 eV confirm the positively charged states of the Fe species (Fig. S9b). No zero-valent Fe was detected, implying that the Fe atoms are bonding with the surrounding atoms. The N 1 *s* spectrum of Fe-CNS(O) contains four contributions including pyridinic- (398.5 eV), pyrrolic- (399.2 eV), graphitic- (400.3 eV), and oxidized-N (402.1 eV), respectively (Fig. 3**g**). The enhanced relative intensities of metal–N signal (398.8 eV) in Fe-CNS(O) compared with bare Fe-CNS implies that Fe and N can mutually stabilize in carbon materials by the formation of Fe–N bonds. The O 1 *s* XPS spectrum of Fe-CNS(O) is featured by two deconvoluted peaks located at 530.7 and 531.9 eV, which are respectively attributed to C═O (O–C═O) and C–O–C (C–OH) bonding. The major peak (284.8 eV) in the C 1 *s* spectrum of Fe-CNS(O) is ascribed to aromatic C═C bonding. The other signals at 285.6, 286.1, and 288.9 eV could be assigned to C–OH, C–O–C, and C═O, respectively (Fig. 3**h**) [41,42]. Collectively, Fig. 3**i** schematically depicts the atomic structure of Fe-CNS (O) in facilitating the 2e⁻ ORR process.

3.3. Electrochemical performance evaluation of Fe-CNS(O) catalyst

The ORR performance of the Fe-CNS(O) catalyst was first evaluated on a RRDE at 1600 rpm in an O_2-saturated KOH electrolyte (0.1 M). The Pt ring electrode was held at 1.2 V to quantify the amount of H_2O_2 produced on the disk electrode. The Fe-CNS(O), graphite rod, and saturated calomel electrode was employed as the working electrode, counter electrode, and reference electrode, respectively. The reference electrode was calibrated in advance. The collection efficiency of RRDE was calibrated to be 23.7%. Fig. 4a shows the polarization curves of CNS, Fe-CNS, and Fe-CNS(O) electrodes, which are featured by the oxygen reduction current measured on the disk electrode (solid lines) and the H_2O_2 oxidation current on the Pt ring electrode (dashed lines). The Fe-CNS(O) electrode exhibits the highest onset potential (E_{onset}) at ~0.7 V *vs.* RHE, approaching the theoretical thermodynamic value allowed to initiate the alkaline 2e⁻ ORR process. As depicted in Fig. 4b, the Fe-CNS(O) electrode affords an advanced H_2O_2 selectivity (~92% from 0.4 to 0.8 V). In contrast, both CNS and Fe-CNS counterparts exhibit a lower H_2O_2 selectivity (<65%) within the same potential range.

To further elucidate the origin of the superior 2e⁻ ORR performance of Fe-CNS(O) material, the reaction kinetics and electrochemical active surface area of the catalysts were evaluated (Fig. S10 and S11). The Fe-CNS(O) presents faster ORR kinetics, showing a Tafel slope of 107.9 mV dec⁻¹ (Fig. 4c). The number of transferred electrons in given voltage intervals is close to 2, substantiating that its ORR process is dominated by a 2e⁻ pathway with H_2O_2 as the main product (Fig. S12). Moreover, linear sweep voltammetry measurements of electrocatalysts were carried out on rotating disk electrode at varied speeds to analyze the Koutecký–Levich curve (Fig. S13). The slope relating to Fe-CNS(O) is closer to the pathway of two-electron reaction.

The long-term stability during H_2O_2 generation was further examined in the O_2-saturated KOH (0.1 M) at a constant applied potential of 0.3 V *vs.* RHE. Upon continuous chronoamperometry testing for ~14 h, the Fe-CNS(O) electrode still maintains stable activity (Fig. 4d). No significant current decay could be observed after 3000 cycles, suggestive
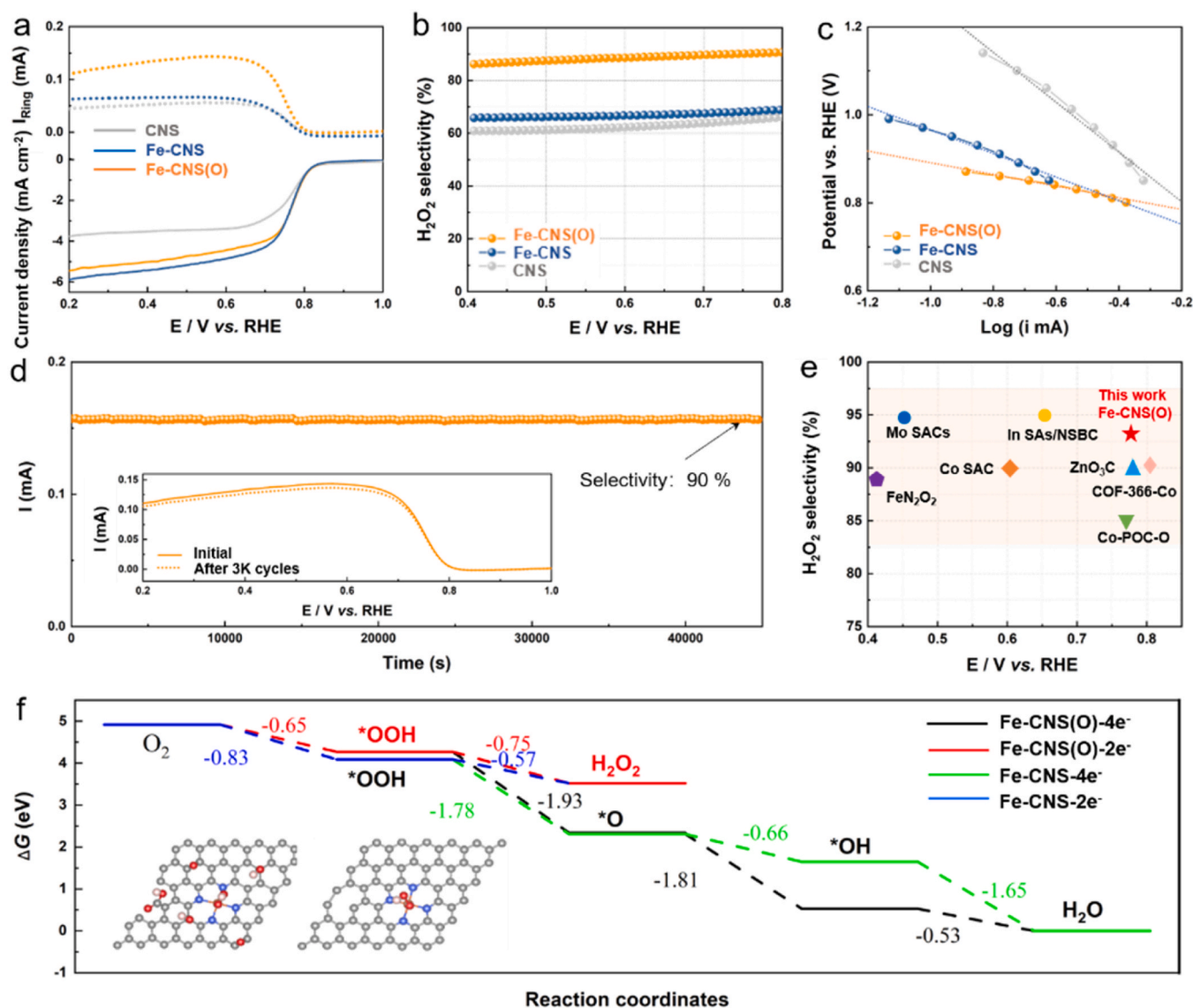

Fig. 4. Electrocatalytic ORR performance of Fe-CNS(O) loaded RRDE in 0.1 M KOH. (a) Polarization curves of CNS, Fe-CNS and Fe-CNS(O) recorded at 1600 rpm and a scan rate of 10 mV s⁻¹, showing the ORR current density on the disk (j_{disk}) and H_2O_2 oxidation current on the ring electrode (I_{ring}). (b) The calculated H_2O_2 selectivity. (c) Corresponding Tafel plots for the H_2O_2 production of CNS, Fe-CNS and Fe-CNS(O). (d) Stability measurement of Fe-CNS(O) catalyst at a fixed disk potential of 0.6 V *vs.* RHE. (e) The H_2O_2 selectivity of Fe-CNS(O) comparison with recently reported catalysts. (f) Free energy diagram for ORR on Fe-CNS and Fe-CNS(O), including the 4e⁻ and 2e⁻ pathways.

of good maintenance of catalytic selectivity (Fig. 4**d** inset; Fig. S14). The post-mortem XRD and XPS results of Fe-CNS(O) also display negligible changes in comparison with its status prior to the reaction (Fig. S15). Such a robustness is one of the keys for practical usage. As for the overpotential and selectivity performances, Fe-CNS(O) compares favorably with the reported single-atomic electrocatalysts tested within alkaline media (Fig. 4**e**) [17,20,43–46].

The trigger of two-electron pathway reaction to generate H_2O_2 is closely related to the binding strength between the catalytic site and OOH* intermediate. In terms of an ideal H_2O_2 electrocatalyst, the adsorption of OOH* need to be neither too strong nor too weak, which enables favorable activity and selectivity [16]. To elucidate the effect of O-coordination structure on the ORR pathway, first-principles calculations based on density functional theory (DFT) method were performed. Two typical atomic models were constructed, namely, Fe-CNS and

Fe-CNS(O). ORR intermediates (*e.g.*, OOH*, O* and OH*) were positioned at varied binding sites to determine the most stable adsorption configuration (Fig. S16 and S17). The free energy diagram of $2e^-/4e^-$ ORR pathway intermediates on Fe-CNS and Fe-CNS(O) at 0 V is depicted (Fig. 4**f**; Table S3). The following competing reactions is related to the trends toward $2e^-/4e^-$ pathway:

$$*OOH + (H^+ + e^-) \rightarrow *O + H_2O \tag{1}$$

$$*OOH + (H^+ + e^-) \rightarrow H_2O_2 \tag{2}$$
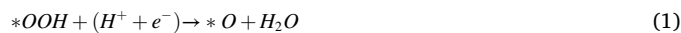
The formation of OOH* is energetically favorable to render a negative free energy change. Once the OOH* intermediate is generated, it could either be further hydrogenated to form an O* species and release a H_2O molecule *via* a $4e^-$ pathway, or proceed to produce an H_2O_2 molecule following a $2e^-$ route [47,48]. The four-electron and
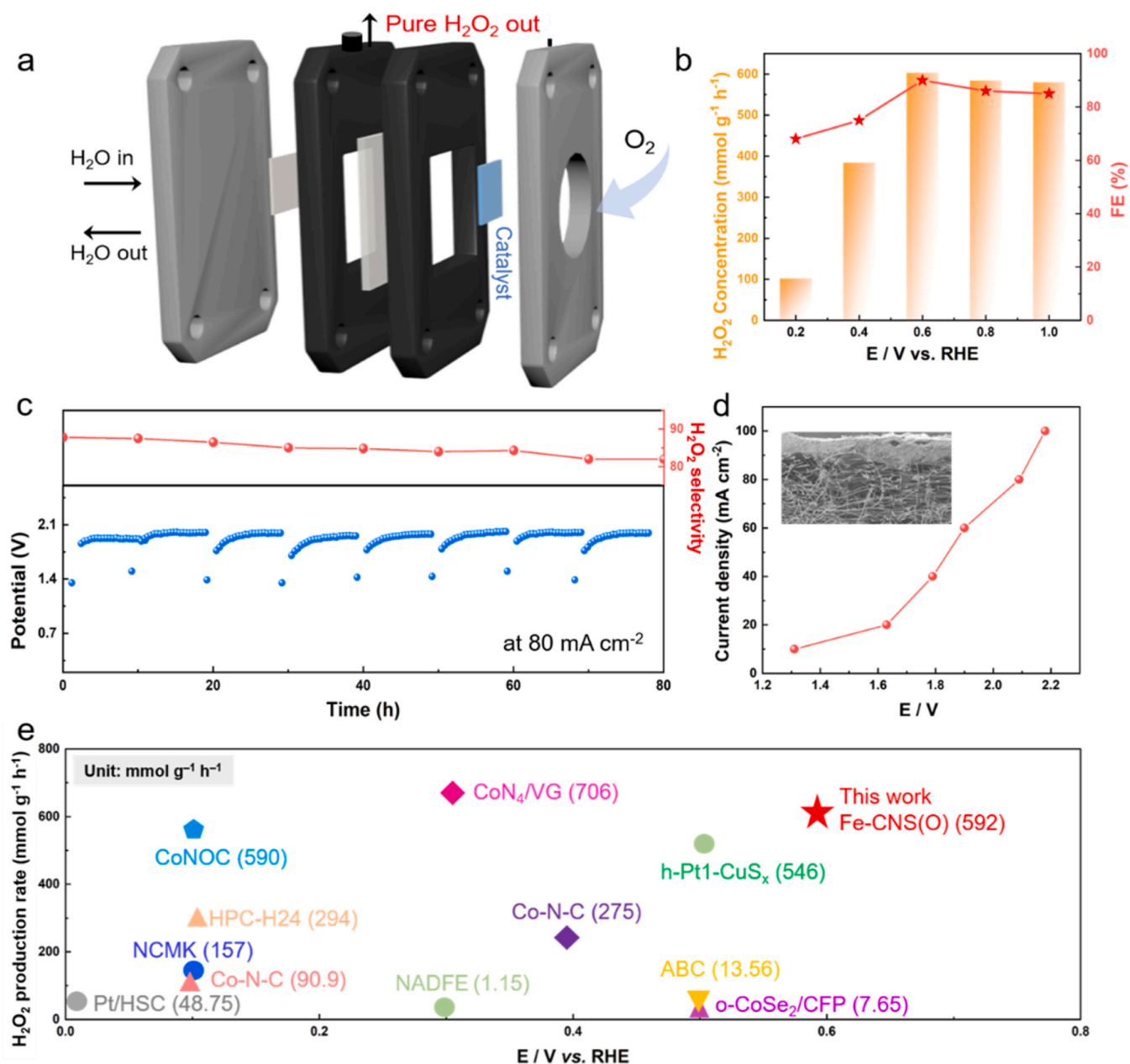

Fig. 5. Practical synthesis of H_2O_2 solution in a flow cell using the single-atomic Fe-dispersed Janus electrode as the cathode. (a) Schematic illustration of the flow cell using the single-atomic Fe-dispersed Janus GDE as the cathode. (b) H_2O_2 production rate and FE as a function of current density. (c) Stability measurement of the Fe-CNS(O) Janus GDE at a current density of 80 mA cm^{-2}. (d) LSVs of Fe-CNS(O) Janus GDE. (e) H_2O_2 production rate of flow cell utilizing Fe-CNS(O) electrode compared with previously reported systems.

two-electron paths of rate-determining step of Fe-CNS(O) are different, from *OH to H_2O and from O_2 to *OOH, respectively. It could be clearly observed in Fig. 4f that the driving force from O_2 to *OOH is larger, and the reaction is spontaneous more rapidly, so that the reaction of Fe-CNS(O) is inclined to the two-electron path.

3.4. Continuous H_2O_2 generation in flow cell using the Janus GDE

The RRDE testing has suggested a favorable catalytic activity, selectivity, and stability of the Fe-CNS(O) material, rendering it a reliable candidate for practical H_2O_2 synthesis. In terms of device-wise consideration, the poor gas-diffusion efficiency and severe H_2O_2 accumulation in a ring disk electrode or an H-cell configuration have posed grand hurdle in boosting the H_2O_2 productivity to meet application demands. To this end, our designed Janus GDE affording a catalytic Fe-CNS(O) layer was employed to equip into a typical flow cell reactor. As illustrated in Fig. 5a, a proton exchange membrane is inserted to separate the anode from the cathode to avoid the crossover of substances. O_2 gas with a flow rate of 5 mL min^{-1} is directly fed into the cathode gas chamber. Favorable O_2 transport could be achieved owing to the ample pore structure and unilateral oxygenophilic feature of the Janus GDE, enabling a high H_2O_2 output of 592 mmol g^{-1} h^{-1} at a potential of 0.6 V *vs.* RHE (Fig. 5b). The electrons consumed over the electrode are mainly responsible for the generation of H_2O_2, showing a Faradaic efficiency (FE$_{H2O2}$) of over 90% at 0.6 V *vs.* RHE. To investigate the capability in enhancing the catalytic activity by favorable GDE design, H_2O_2 yield comparison was drawn using Fe-CNS(O)-based electrodes with/without the gas-attracting layer. Under the same testing conditions, the yield at the Janus electrode was markedly increased (Fig. S18). In further contexts, electrochemical impedance spectroscopy profiles were collected to decipher the advanced performance of the Janus electrode. As shown in Fig. S19, The Janus electrode readily displays both weakened mass transport resistance and charge transfer resistance. To showcase the merits of the Janus GDE pertaining to electrochemical durability, H_2O_2 can be sustainably produced for 80 h at a current density of 80 mA cm^{-2} (Fig. 5c; Fig. S20). Upon collecting the polarization curves under different catalyst loadings, an optimal loading could be determined (Fig. S21). The H_2O_2 selectivity can be consistently maintained at the meantime reaching a high value of 82%– 93%. By applying various oxygen concentrations, the oxygen reduction current on GDE shows no discernible change, indicating that the oxygen mass transfer in ORR was primarily determined by gas-phase diffusion rather than dissolved oxygen in the solution (Fig. 5d; Fig. S22). As compared to one of our previously published studies [19], the favorable performance of present GDE regarding the H_2O_2 productivity (1.96 mg cm^{-2} h^{-1} herein *vs.* 1.57 mg cm^{-2} h^{-1} in ref. 19) could be attributed to certain advances in the electrode design and application scenarios. Specifically, at a microscopic scale, Fe-CNS(O) not only affords a favorable 2e$^-$ ORR selectivity but also benefits for the aqueous electrolyte wetting; in a macroscopic level, the catalytic layer is formed by spray coating of catalyst inks instead of brush coating, thus ensuring a spatially uniform catalyst loading over the electrode (Table S4). Moreover, in the present work, the employment of H_2O_2 produced from a flow cell reactor rather than an H-cell electrolyzer to allow the *in situ* antibiotic degradation was systematically demonstrated - we acknowledge that a comprehensive exploration in this direction could be envisaged based on the current results. The advancement of the present GDE is also reflected by its device durability, which readily enables durable operations for 80 h under a current density of 80 mA cm^{-2} while maintaining on-demand H_2O_2 production concentrations. This is apparently superior to that (50 h under 60 mA cm^{-2}) from the previous report. Equally importantly, our single-atomic Fe-dispersed Janus GDE represents one of the state-of-the-art electrode devices designed for robust H_2O_2 generation, where the performances pertaining to H_2O_2 production and operation stability surpass those of related studies (Fig. 5e; Table S5) [39,44, 48–54]. Note that the environmental relevance and significance of

current GDE design in on-site producing H_2O_2 have been in target shown, thereby holding promise for the application of 2e$^-$ ORR science and technology in water environmental remediation.

3.5. Wastewater remediation using electrochemically generated H_2O_2

The sustainably produced H_2O_2 could be directly utilized for on-demand wastewater remediation. Fig. 6a summarizes the comparison of degradation rates between the prepared Fe-CNS and Fe-CNS(O), where an optimized catalyst could be pinpointed. To evaluate the levofloxacin (LVF; 10 mg L^{-1}) degradation performance by the produced H_2O_2, 3D excitation-emission matrix (3DEEM) fluorescence spectra were collected (Fig. S23), clearly showing the vanished LVF signal after 90 min. More encouragingly, our Janus GDE [denoted as Fe-CNS(O)@J-GDE] presents the highest LVF degradation efficiency among the as-assembled electrodes under identical testing conditions (Fig. 6b). As further indicated in Fig. 6c, the cyclic degradation tests of such an electrode merely show a negligible efficiency decline after five repetitive cycles, verifying the robustness and effectiveness for practical water purification. Supplementary DFT simulations were performed to offer in-depth insight into the interaction between the oxygen-decorated Fe single atoms and antibiotic molecules. Fig. 6d show the fully relaxed atomic configurations of LVF over Fe-CNS and Fe-CNS(O), respectively, with the corresponding adsorption energy (E_{ads}) values calculated. It could be seen that the scenario of LVF binding on Fe-CNS(O) possesses a more negative E_{ads} (Fig. S24). In this respect, it could be speculated that the free radicals generated both at the electrode surface and at the bulk solution with the presence of H_2O_2 play a leading role in the oxidative degradation.

4. Conclusion

In summary, we have designed a scalable Janus three-phase electrode equipped with single-atomic Fe moieties to realize unimpeded gaseous O_2 transport and entrapment owing to unilateral super-aerophilicity, accordingly augmenting the efficiency of electrochemical production of H_2O_2. The successful implementation of Fe-CNS(O) renders impressive 2e$^-$ ORR selectivity (92%). The devised Janus electrode tackles the bottleneck of low current density limitation, readily enabling stable operations under high current densities of 20 – 200 mA cm^{-2} while maintaining on-demand H_2O_2 production concentrations. Benefiting from these geometrical and physiochemical superiorities, *in situ* produced H_2O_2 enables the effective treatment of model water pollutants including RhB and LVF, achieving satisfactory degradation efficiency higher than 95%.

CRediT authorship contribution statement

Yuhan Wu: Data curation, Investigation, Formal analysis, Writing – original draft. **Yifei Wang:** Formal analysis, Project administration, Resources, Writing – review & editing. **Ruyan Chen:** Formal analysis, Validation, Software, Writing – original draft. **Jiaqing Xu:** Investigation, Data curation. **Yifei Wang:** Investigation, Methodology. **Hangyuan Zhang:** Investigation. **Yifan Ding:** Formal analysis, Validation. **Beibei Li:** Investigation, Writing – original draft. **Shuying Dong:** Resources, Validation, Writing – review & editing. **Shixue Dou:** Formal analysis, Software, Supervision. **Xiao Zhang:** Formal analysis, Supervision, Writing – review & editing. **Jingyu Sun:** Project administration, Supervision, Funding acquisition, Writing – review & editing. **Jianhui Sun:** Conceptualization, Project administration, Resources, Writing – review & editing.

Declaration of Competing Interest

The authors declare that they have no known competing financial interests or personal relationships that could have appeared to influence
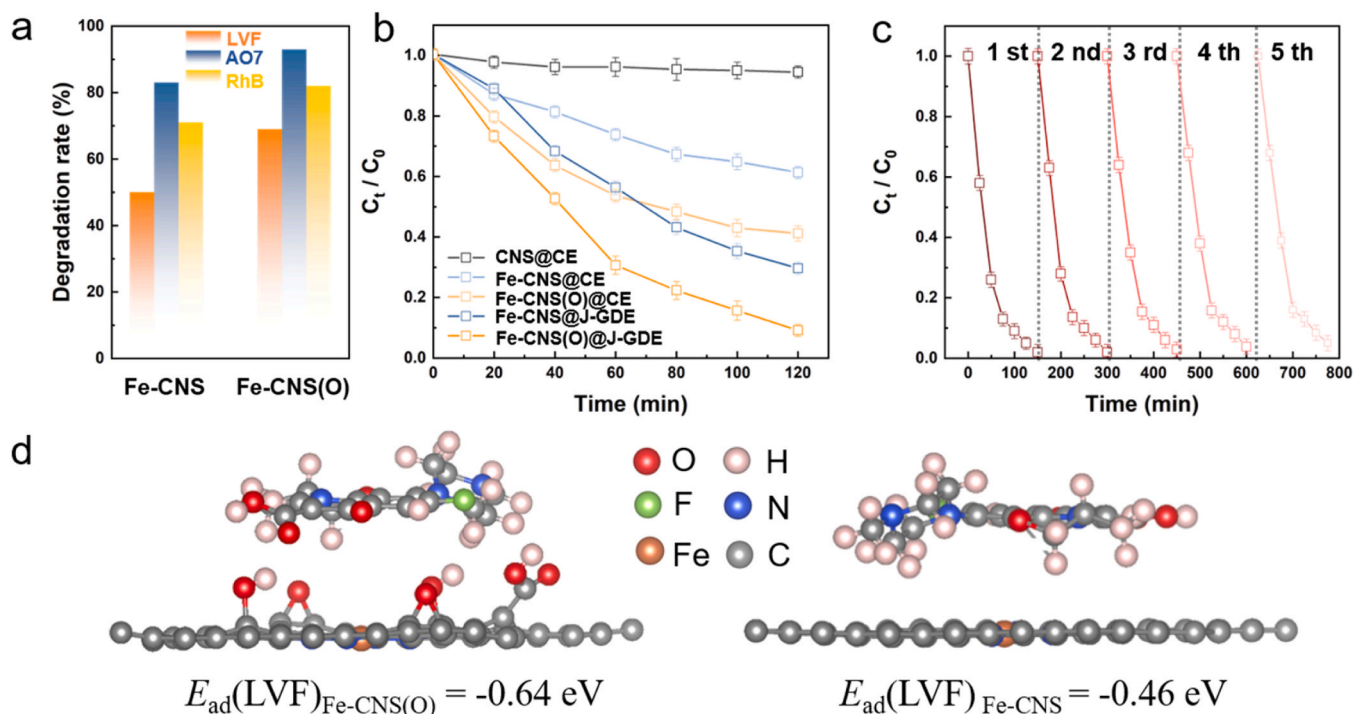
Fig. 6. Proposed degradation pathways of LVF by on-site produced H_2O_2 in $2e^-$ ORR system. (a) Summary of degradation efficiency of Fe-CNS(O) (dye: RhB and AO7; antibiotic: LVF). (b) Comparison of LVF removal rate between Fe-CNS(O) and the control samples (*CE* denotes the conventional electrode: a conventionally coated electrode that was completely immersed in the electrolyte system; *J-GDE* denotes our Janus gas diffusion electrode, where the gas-attraction layer is exposed to air and the catalyst layer is in contact with the electrolyte). (c) Cyclic degradation performance of Fe-CNS(O) toward LVF. (d) Optimized structure of Fe-CNS(O) for adsorption of macromolecular antibiotics.

the work reported in this paper.

Data availability

Data will be made available on request.

Appendix A. Supporting information

Supplementary data associated with this article can be found in the online version at doi:10.1016/j.apcatb.2023.123533.

References

[1] J.M. Campos-Martin, G. Blanco-Brieva, J.L. Fierro, Hydrogen peroxide synthesis: an outlook beyond the anthraquinone process, Angew. Chem. Int. Ed. 45 (2006) 6962–6984.

[2] Z. Chen, S. Chen, S. Siahrostami, P. Chakthranont, C. Hahn, D. Nordlund, S. Dimosthenis, J.K. Nørskov, Z. Bao, T.F. Jaramillo, Development of a reactor with carbon catalysts for modular-scale, low-cost electrochemical generation of H_2O_2, React. Chem. Eng. 2 (2017) 239–245.

[3] C.A. Martinez-Huitle, S. Ferro, Electrochemical oxidation of organic pollutants for the wastewater treatment: direct and indirect processes, Chem. Soc. Rev. 35 (2006) 1324–1340.

[4] S. Siahrostami, A. Verdaguer-Casadevall, M. Karamad, D. Deiana, P. Malacrida, B. Wickman, M. Escudero-Escribano, E.A. Paoli, R. Frydendal, T.W. Hansen, I. Chorkendorff, I.E. Stephens, J. Rossmeisl, Enabling direct H_2O_2 production through rational electrocatalyst design, Nat. Mater. 12 (2013) 1137–1143.

[5] J. Filippi, H.A. Miller, L. Nasi, M.V. Pagliaro, A. Marchionni, M. Melchionna, P. Fornasiero, F. Vizza, Optimization of H_2O_2 production in a small-scale off-grid buffer layer flow cell equipped with Cobalt@N-doped graphitic carbon core–shell nanohybrid electrocatalyst, Mater. Today Energy 29 (2022), 101092.

[6] S. Yang, A. Verdaguer-Casadevall, L. Arnarson, L. Silvioli, V. Čolić, R. Frydendal, J. Rossmeisl, I. Chorkendorff, I.E.L. Stephens, Toward the decentralized electrochemical production of H_2O_2: a focus on the catalysis, ACS Catal. 8 (2018) 4064–4081.

[7] C. Xia, Y. Xia, P. Zhu, L. Fan, H. Wang, Direct electrosynthesis of pure aqueous H_2O_2 solutions up to 20% by weight using a solid electrolyte, Science 366 (2019) 226–231.

[8] J.S. Jirkovsky, I. Panas, E. Ahlberg, M. Halasa, S. Romani, D.J. Schiffrin, Single atom hot-spots at Au-Pd nanoalloys for electrocatalytic H_2O_2 production, J. Am. Chem. Soc. 133 (2011) 19432–19441.

[9] C.H. Choi, H.C. Kwon, S. Yook, H. Shin, H. Kim, M. Choi, Hydrogen peroxide synthesis via enhanced two-electron oxygen reduction pathway on carbon-coated Pt surface, J. Phys. Chem. C 118 (2014) 30063–30070.

[10] C.H. Choi, M. Kim, H.C. Kwon, S.J. Cho, S. Yun, H.T. Kim, K.J. Mayrhofer, H. Kim, M. Choi, Tuning selectivity of electrochemical reactions by atomically dispersed platinum catalyst, Nat. Commun. 7 (2016) 10922.

[11] S. Yang, J. Kim, Y.J. Tak, A. Soon, H. Lee, Single-atom catalyst of platinum supported on titanium nitride for selective electrochemical reactions, Angew. Chem. Int. Ed. 55 (2016) 2058–2062.

[12] Y.L. Wang, S. Gurses, N. Felvey, A. Boubnov, S.S. Mao, C.X. Kronawitter, In situ deposition of pd during oxygen reduction yields highly selective and active electrocatalysts for direct H_2O_2 production, ACS Catal. 9 (2019) 8453–8463.

[13] D. Liu, Q. He, S. Ding, L. Song, Structural regulation and support coupling effect of single-atom catalysts for heterogeneous catalysis, Adv. Energy Mater. 10 (2020).

[14] J. Liu, Z. Gong, M. Yan, G. He, H. Gong, G. Ye, H. Fei, Electronic structure regulation of single-atom catalysts for electrochemical oxygen reduction to H_2O_2, Small (2021), e2103824.

[15] C.X. Zhao, B.Q. Li, J.N. Liu, Q. Zhang, Intrinsic electrocatalytic activity regulation of M-N-C single-atom catalysts for the oxygen reduction reaction, Angew. Chem. Int. Ed. 60 (2021) 4448–4463.

[16] X. Guo, S. Lin, J. Gu, S. Zhang, Z. Chen, S. Huang, Simultaneously achieving high activity and selectivity toward two-electron O_2 electroreduction: the power of single-atom catalysts, ACS Catal. 9 (2019) 11042–11054.

[17] C. Tang, Y. Jiao, B. Shi, J.N. Liu, Z. Xie, X. Chen, Q. Zhang, S.Z. Qiao, Coordination tunes selectivity: two-electron oxygen reduction on high-loading molybdenum single-atom catalysts, Angew. Chem. Int. Ed. 59 (2020) 9171–9176.

[18] H. Gong, Z. Wei, Z. Gong, J. Liu, G. Ye, M. Yan, J. Dong, C. Allen, J. Liu, K. Huang, R. Liu, G. He, S. Zhao, H. Fei, Low-coordinated CoNC on oxygenated graphene for efficient electrocatalytic H$_2$O$_2$ production, Adv. Funct. Mater. 32 (2022) 2106886.

[19] Y. Wu, Y. Ding, X. Han, B. Li, Y. Wang, S. Dong, Q. Li, S. Dou, J. Sun, J. Sun, Modulating coordination environment of Fe single atoms for high-efficiency all-pH-tolerated H$_2$O$_2$ electrochemical production, Appl. Catal. B Environ. 315 (2022) 121578.

[20] Y. Jia, Z. Xue, J. Yang, Q. Liu, J. Xian, Y. Zhong, Y. Sun, X. Zhang, Q. Liu, D. Yao, G. Li, Tailoring the electronic structure of an atomically dispersed zinc electrocatalyst: coordination environment regulation for high selectivity oxygen reduction, Angew. Chem. Int. Ed. 61 (2022), e202110838.

[21] E. Jung, H. Shin, B.H. Lee, V. Efremov, S. Lee, H.S. Lee, J. Kim, W. Hooch Antink, S. Park, K.S. Lee, S.P. Cho, J.S. Yoo, Y.E. Sung, T. Hyeon, Atomic-level tuning of Co-N-C catalyst for high-performance electrochemical H$_2$O$_2$ production, Nat. Mater. 19 (2020) 436–442.

[22] Z. Teng, Q. Zhang, H. Yang, K. Kato, W. Yang, Y.-R. Lu, S. Liu, C. Wang, A. Yamakata, C. Su, B. Liu, T. Ohno, Atomically dispersed antimony on carbon nitride for the artificial photosynthesis of hydrogen peroxide, Nat. Catal. 4 (2021) 374–384.

[23] C.X. Zhao, J.N. Liu, J. Wang, D. Ren, B.Q. Li, Q. Zhang, Recent advances of noble-metal-free bifunctional oxygen reduction and evolution electrocatalysts, Chem. Soc. Rev. 50 (2021) 7745–7778.

[24] P. Cao, X. Quan, K. Zhao, X. Zhao, S. Chen, H. Yu, Durable and selective electrochemical H$_2$O$_2$ synthesis under a large current enabled by the cathode with highly hydrophobic three-phase architecture, ACS Catal. 11 (2021) 13797–13808.

[25] J. Xu, X. Zheng, Z. Feng, Z. Lu, Z. Zhang, W. Huang, Y. Li, D. Vuckovic, Y. Li, S. Dai, G. Chen, K. Wang, H. Wang, J.K. Chen, W. Mitch, Y. Cui, Organic wastewater treatment by a single-atom catalyst and electrolytically produced H$_2$O$_2$, Nat. Sustain. 4 (2020) 233–241.

[26] Z. Lu, G. Chen, S. Siahrostami, Z. Chen, K. Liu, J. Xie, L. Liao, T. Wu, D. Lin, Y. Liu, T.F. Jaramillo, J.K. Nørskov, Y. Cui, High-efficiency oxygen reduction to hydrogen peroxide catalysed by oxidized carbon materials, Nat. Catal. 1 (2018) 156–162.

[27] B. Sabri Rawah, M. Alblooshi, W. Li, Electro-synthesis of pure aqueous H$_2$O$_2$ on nitrogen-doped carbon in a solid electrolyte flow cell without using anion exchange membrane, Chem. Eng. J. 466 (2023) 143282.

[28] Y.J. Sa, J.H. Kim, S.H. Joo, Active edge-site-rich carbon nanocatalysts with enhanced electron transfer for efficient electrochemical hydrogen peroxide production, Angew. Chem. Int. Ed. 58 (2019) 1100–1105.

[29] M. Wang, N. Zhang, Y. Feng, Z. Hu, Q. Shao, X. Huang, Partially pyrolyzed binary metal-organic framework nanosheets for efficient electrochemical hydrogen peroxide synthesis, Angew. Chem. Int. Ed. 59 (2020) 14373–14377.

[30] Z. Lin, Q. Zhang, J. Pan, C. Tsounis, A.A. Esmailpour, S. Xi, H.Y. Yang, Z. Han, J. Yun, R. Amal, X. Lu, Atomic Co decorated free-standing graphene electrode assembly for efficient hydrogen peroxide production in acid, Energy Environ. Sci. 15 (2022) 1172–1182.

[31] P. Liu, B. Chen, C. Liang, W. Yao, Y. Cui, S. Hu, P. Zou, H. Zhang, H.J. Fan, C. Yang, Tip-enhanced electric field: a new mechanism promoting mass transfer in oxygen evolution reactions, Adv. Mater. 33 (2021) 2007377.

[32] Q. Yang, Y. Guo, B. Yan, C. Wang, Z. Liu, Z. Huang, Y. Wang, Y. Li, H. Li, L. Song, J. Fan, C. Zhi, Hydrogen-substituted graphdiyne ion tunnels directing concentration redistribution for commercial-grade dendrite-free zinc anodes, Adv. Mater. 32 (2020) 2001755.

[33] J.N. Liu, C.X. Zhao, D. Ren, J. Wang, R. Zhang, S.H. Wang, C. Zhao, B.Q. Li, Q. Zhang, Preconstructing asymmetric interface in air cathodes for high-performance rechargeable Zn-air batteries, Adv. Mater. 34 (2022), e2109407.

[34] J. Ding, H. Zhang, H. Zhou, J. Feng, X. Zheng, C. Zhong, E. Paek, W. Hu, D. Mitlin, Sulfur-grafted hollow carbon spheres for potassium-ion battery anodes, Adv. Mater. 31 (2019), e1900429.

[35] J. Liu, N.P. Wickramaratne, S.Z. Qiao, M. Jaroniec, Molecular-based design and emerging applications of nanoporous carbon spheres, Nat. Mater. 14 (2015) 763–774.

[36] S. Chen, Z. Chen, S. Siahrostami, D. Higgins, D. Nordlund, D. Sokaras, T.R. Kim, Y. Liu, X. Yan, E. Nilsson, R. Sinclair, J.K. Norskov, T.F. Jaramillo, Z. Bao, Designing boron nitride islands in carbon materials for efficient electrochemical synthesis of hydrogen peroxide, J. Am. Chem. Soc. 140 (2018) 7851–7859.

[37] S. Kralj, F. Longobardo, D. Iglesias, M. Bevilacqua, C. Tavagnacco, A. Criado, J. J. Delgado Jaen, D. Makovec, S. Marchesan, M. Melchionna, M. Prato, P. Fornasiero, Ex-solution synthesis of Sub-5-nm FeOx nanoparticles on mesoporous hollow N,O-doped carbon nanoshells for electrocatalytic oxygen reduction, ACS Appl. Nano Mater. 2 (2019) 6092–6097.

[38] X. Sheng, N. Daems, B. Geboes, M. Kurttepeli, S. Bals, T. Breugelmans, A. Hubin, I. F.J. Vankelecom, P.P. Pescarmona, N-doped ordered mesoporous carbons prepared by a two-step nanocasting strategy as highly active and selective electrocatalysts for the reduction of O$_2$ to H$_2$O$_2$, Appl. Catal. B Environ. 176–177 (2015) 212–224.

[39] Y. Sun, I. Sinev, W. Ju, A. Bergmann, S. Dresp, S. Kühl, C. Spöri, H. Schmies, H. Wang, D. Bernsmeier, B. Paul, R. Schmack, R. Kraehnert, B. Roldan Cuenya, P. Strasser, Efficient electrochemical hydrogen peroxide production from molecular oxygen on nitrogen-doped mesoporous carbon catalysts, ACS Catal. 8 (2018) 2844–2856.

[40] Y. Chen, Z. Li, Y. Zhu, D. Sun, X. Liu, L. Xu, Y. Tang, Atomic Fe dispersed on N-doped carbon hollow nanospheres for high-efficiency electrocatalytic oxygen reduction, Adv. Mater. 31 (2019) 1806312.

[41] H.W. Kim, M.B. Ross, N. Kornienko, L. Zhang, J. Guo, P. Yang, B.D. McCloskey, Efficient hydrogen peroxide generation using reduced graphene oxide-based oxygen reduction electrocatalysts, Nat. Catal. 1 (2018) 282–290.

[42] Z. Lu, G. Chen, S. Siahrostami, Z. Chen, K. Liu, J. Xie, L. Liao, T. Wu, D. Lin, Y. Liu, T.F. Jaramillo, J.K. Nørskov, Y. Cui, High-efficiency oxygen reduction to hydrogen peroxide catalysed by oxidized carbon materials, Nat. Catal. 1 (2018) 156–162.

[43] B.Q. Li, C.X. Zhao, J.N. Liu, Q. Zhang, Electrosynthesis of hydrogen peroxide synergistically catalyzed by atomic Co-N(x) -C sites and oxygen functional groups in noble-metal-free electrocatalysts, Adv. Mater. 31 (2019), e1808173.

[44] J. Gao, Hb Yang, X. Huang, S.-F. Hung, W. Cai, C. Jia, S. Miao, H.M. Chen, X. Yang, Y. Huang, T. Zhang, B. Liu, Enabling direct H$_2$O$_2$ production in acidic media through rational design of transition metal single atom catalyst, Chem 6 (2020) 658–674.

[45] F. Ma, S. Wang, X. Liang, C. Wang, F. Tong, Z. Wang, P. Wang, Y. Liu, Y. Dai, Z. Zheng, B. Huang, Ni$_3$B as a highly efficient and selective catalyst for the electrosynthesis of hydrogen peroxide, Appl. Catal. B Environ. 279 (2020) 119371.

[46] E. Zhang, L. Tao, J. An, J. Zhang, L. Meng, X. Zheng, Y. Wang, N. Li, S. Du, J. Zhang, D. Wang, Y. Li, Engineering the local atomic environments of indium single-atom catalysts for efficient electrochemical production of hydrogen peroxide, Angew. Chem. Int. Ed. 61 (2022), e202117347.

[47] S. Chen, T. Luo, X. Li, K. Chen, J. Fu, K. Liu, C. Cai, Q. Wang, H. Li, Y. Chen, C. Ma, L. Zhu, Y.R. Lu, T.S. Chan, M. Zhu, E. Cortes, M. Liu, Identification of the highly active Co-N(4) coordination motif for selective oxygen reduction to hydrogen peroxide, J. Am. Chem. Soc. 144 (2022) 14505–14516.

[48] H. Sheng, A.N. Janes, R.D. Ross, D. Kaiman, J. Huang, B. Song, J.R. Schmidt, S. Jin, Stable and selective electrosynthesis of hydrogen peroxide and the electro-Fenton process on CoSe$_2$ polymorph catalysts, Energy Environ. Sci. 13 (2020) 4189–4203.

[49] Y. Liu, X. Quan, X. Fan, H. Wang, S. Chen, High-yield electrosynthesis of hydrogen peroxide from oxygen reduction by hierarchically porous carbon, Angew. Chem. Int. Ed. 54 (2015) 6837–6841.

[50] L.G. Xie, S. Niyomchon, A.J. Mota, L. Gonzalez, N. Maulide, Metal-free intermolecular formal cycloadditions enable an orthogonal access to nitrogen heterocycles, Nat. Commun. 7 (2016) 10914.

[51] Y. Sun, S. Li, Z.P. Jovanov, D. Bernsmeier, H. Wang, B. Paul, X. Wang, S. Kuhl, P. Strasser, Structure, activity, and faradaic efficiency of nitrogen-doped porous carbon catalysts for direct electrochemical hydrogen peroxide production, ChemSusChem 11 (2018) 3388–3395.

[52] R. Shen, W. Chen, Q. Peng, S. Lu, L. Zheng, X. Cao, Y. Wang, W. Zhu, J. Zhang, Z. Zhuang, C. Chen, D. Wang, Y. Li, High-concentration single atomic Pt sites on hollow CuSx for selective O$_2$ reduction to H$_2$O$_2$ in acid solution, Chem 5 (2019) 2099–2110.

[53] Y. Sun, L. Silvioli, N.R. Sahraie, W. Ju, J. Li, A. Zitolo, S. Li, A. Bagger, L. Arnarson, X. Wang, T. Moeller, D. Bernsmeier, J. Rossmeisl, F. Jaouen, P. Strasser, Activity-selectivity trends in the electrochemical production of hydrogen peroxide over single-site metal-nitrogen-carbon catalysts, J. Am. Chem. Soc. 141 (2019) 12372–12381.

[54] C. Tang, L. Chen, H. Li, L. Li, Y. Jiao, Y. Zheng, H. Xu, K. Davey, S.Z. Qiao, Tailoring acidic oxygen reduction selectivity on single-atom catalysts via modification of first and second coordination spheres, J. Am. Chem. Soc. 143 (2021) 7819–7827.